Applied Physics Letters

Anisotropic dielectric function, direction dependent bandgap energy, band order, and indirect to direct gap crossover in α-$(Al_xGa_{1-x})_2O_3$ ($0 \leq x \leq 1$)

Cite as: Appl. Phys. Lett. **121**, 052101 (2022); https://doi.org/10.1063/5.0087602
Submitted: 07 February 2022 • Accepted: 25 June 2022 • Published Online: 01 August 2022

Matthew Hilfiker, Ufuk Kilic, Megan Stokey, et al.

AIP Publishing

Applied Physics Letters ARTICLE scitation.org/journal/apl

Anisotropic dielectric function, direction dependent bandgap energy, band order, and indirect to direct gap crossover in α-$(Al_xGa_{1-x})_2O_3$ $(0 \le x \le 1)$

Cite as: Appl. Phys. Lett. **121**, 052101 (2022); doi: 10.1063/5.0087602
Submitted: 7 February 2022 · Accepted: 25 June 2022 ·
Published Online: 1 August 2022

Matthew Hilfiker,[1,a)] Ufuk Kilic,[1] Megan Stokey,[1] Riena Jinno,[2,3] Yongjin Cho,[2] Huili Grace Xing,[2,4] Debdeep Jena,[2,4] Rafał Korlacki,[1] and Mathias Schubert[1,5]

AFFILIATIONS

[1]Department of Electrical and Computer Engineering, University of Nebraska-Lincoln, Lincoln, Nebraska 68588, USA
[2]School of Electrical and Computer Engineering, Cornell University, Ithaca, New York 14853, USA
[3]Department of Electronic Science and Engineering, Kyoto University, Kyoto 615-8510, Japan
[4]Department of Material Science and Engineering, Cornell University, Ithaca, New York 14853, USA
[5]Terahertz Materials Analysis Center and Center for III-N Technology, C3NiT–Janzèn, Department of Physics, Chemistry and Biology (IFM), Linköping University, 58183 Linköping, Sweden

Note: This paper is part of the APL Special Collection on Wide- and Ultrawide-Bandgap Electronic Semiconductor Devices.
[a)]**Author to whom correspondence should be addressed:** mhilfiker2@unl.edu. **URL:** http://ellipsometry.unl.edu

ABSTRACT

Mueller matrix spectroscopic ellipsometry is applied to determine anisotropic optical properties for a set of single-crystal rhombohedral structure α-$(Al_xGa_{1-x})_2O_3$ thin films $(0 \le x \le 1)$. Samples are grown by plasma-assisted molecular beam epitaxy on *m*-plane sapphire. A critical-point model is used to render a spectroscopic model dielectric function tensor and to determine direct electronic band-to-band transition parameters, including the direction dependent two lowest-photon energy band-to-band transitions associated with the anisotropic bandgap. We obtain the composition dependence of the direction dependent two lowest band-to-band transitions with separate bandgap bowing parameters associated with the perpendicular ($b_{Eg,\perp} = 1.31$ eV) and parallel ($b_{Eg,||} = 1.61$ eV) electric field polarization to the lattice *c* direction. Our density functional theory calculations indicate a transition from indirect to direct characteristics between α-Ga_2O_3 and α-Al_2O_3, respectively, and we identify a switch in band order where the lowest band-to-band transition occurs with polarization perpendicular to *c* in α-Ga_2O_3 whereas for α-Al_2O_3 the lowest transition occurs with polarization parallel to *c*. We estimate that the change in band order occurs at approximately 40% Al content. Additionally, the characteristic of the lowest energy critical point transition for polarization parallel to *c* changes from M_1 type in α-Ga_2O_3 to M_0 type van Hove singularity in α-Al_2O_3.

Recent research attention has developed to determine materials with an ultra-wide electronic bandgap for future use in high power electronics and ultraviolet optical devices. Of such, the metastable rhombohedral α-phase polymorph of Ga_2O_3 has shown significant promise over the monoclinic structure β-phase[1] due to its potential for high quality growth, lower growth temperature, ability for heteroepitaxial growth on affordable sapphire substrates, and presenting a higher symmetry ($\overline{R3}c$, space group 167).[2–5] To create state-of-the-art high power electronic devices, materials with a high breakdown electric field are required. α-Ga_2O_3 possesses very large direct bandgap energies, which depend on the polarization direction relative to the rhombohedral unit cell, i.e., for polarization perpendicular to the lattice *c* direction, $E_{g,\perp} = 5.46(6)$ eV, and parallel, $E_{g,||} = 5.62(2)$ eV.[6] The critical electric field is proportional to the bandgap energy with the power of 1.83.[7] To further exploit the advantages of α-Ga_2O_3, alloying with the isostructural compound α-Al_2O_3 ($E_g = 9.2$ eV)[8] presents the opportunity to create stable alloys, where the bandgap can be precisely configured between the two binary compounds.[9]

Alloying has been widely used for other material systems such as $Al_xGa_{1-x}N$.[10–14] Recently, a monoclinic β-phase of $(Al_xGa_{1-x})_2O_3$

received substantial interest for potentially providing ultraviolet bandgap capabilities beyond that of the $Al_xGa_{1-x}N$ material system. Successful growth of single-crystal β-$(Al_xGa_{1-x})_2O_3$ has been reported using plasma-assisted molecular beam epitaxy (PAMBE) for alloy concentrations up to $x \leq 0.21$.[15,16] However, the β-phase presents challenges in fabricating high quality aluminum content crystals as α-Al_2O_3 (rhombohedral) and β-Ga_2O_3 (monoclinic) do not share the same crystal structure, possibly limiting the application range for β-$(Al_xGa_{1-x})_2O_3$-based devices. Note that the monoclinic phase of Al_2O_3 is termed as a θ phase and remains obscure. In contrast, alloying rhombohedral α-Ga_2O_3 with rhombohedral α-Al_2O_3 can provide single phase materials with bandgap values ranging between 5.4 and 9.2 eV.[8,17] However, the α-phase is metastable, and stable heteroepitaxial thin films are required.

Recent advances have been made to fabricate α-$(Al_xGa_{1-x})_2O_3$ using a variety of deposition techniques.[18–23] Producing pure α-phase Ga_2O_3 was demonstrated recently by Jinno *et al.* using *m*-plane sapphire substrates which allowed for complete suppression of β-phase formation. Jinno *et al.* were able to grow stable, strain-free, high quality single crystalline α-$(Al_xGa_{1-x})_2O_3$ thin films spanning the full range of Al content ($0 \leq x \leq 1$).[24]

Accurate knowledge of the bandgap properties as a function of the Al content in α-$(Al_xGa_{1-x})_2O_3$ is essential for device design. For α-$(Al_xGa_{1-x})_2O_3$, the band structure reveals characteristic differences vs *x*. For α-Ga_2O_3 and α-Al_2O_3, as shown in our paper here, both the characteristics and the order of the fundamental band-to-band transitions change. α-Ga_2O_3 is indirect while α-Al_2O_3 is a direct semiconductor. Furthermore, in both compounds the band-to-band transitions differ for different polarizations, and the lowest transition in α-Ga_2O_3 is polarized perpendicular to lattice direction *c* while in α-Al_2O_3 the lowest transition is polarized parallel to *c*. Because our samples are strain free, effects of strain are of no concern here.[24] Then, alloying induces order–disorder phenomena that can lead to modifications of band structure properties. For example, complete atomic ordering in, e.g., same-group lattice sites can lead to substantial reduction of bandgap energy, as seen in AlGaInP.[25] Such order–disorder effects further affect the composition dependence of the bandgap energy parameters, which is often approximated by the introduction of a bowing parameter, *b*, in addition to the linear bandgap shift:

$$E_{g,j}(x) = (1-x)E_{g,j}[x=0] + xE_{g,j}[x=1] - b_j x(1-x), \quad (1)$$

where $E_{g,j}[x=0]$, $E_{g,j}[x=1]$, b_j, and *x* are the bandgap energy of α-Ga_2O_3, α-Ga_2O_3, bowing parameter, and aluminum composition, respectively, and $j =$ " $\|$ ", " $\|$ ". Density functional theory (DFT) provides a computational method for investigating these parameters. Wang *et al.* determined formation enthalpies and bandgap energies for both β and α-$(Al_xGa_{1-x})_2O_3$. The authors reported a bowing parameter of 1.6 eV for the α-phase, while noting that different bowing parameters can be associated for the Al content range $0 \leq x \leq 0.5$ ($b_{Eg} = 0.32$ eV) compared to $0.5 \leq x \leq 1$ ($b_{Eg} = 0.74$ eV).[26] Peelaers *et al.* also performed DFT calculation and reported a bowing parameter of 1.87 eV for the α-phase.[17] We note that neither Wang *et al.* nor Peelaers *et al.* discussed the type of the valence bands involved in the lowest transition, nor which order these bands form into the valence band. As we will show in this Letter, the order changes, and hence, bowing parameters should be expressed for transitions that maintain the polarization characteristics, while these do not correspond to the lowest transition throughout the composition range. Instead, there are crossover regions between the type of the lowest transition. Likewise, the characteristic changes from indirect to direct transition.

Optical measurements have been performed to experimentally determine the bandgap values of α-$(Al_xGa_{1-x})_2O_3$. Ito *et al.* epitaxially grew crystalline α-$(Al_xGa_{1-x})_2O_3$ ($0 \leq x \leq 0.81$) on *c*-plane sapphire substrates using spray-assisted mist-CVD. Unpolarized transmission spectra were measured to provide an estimate of the bandgap.[19] Dang *et al.* also applied mist-CVD to grow single-crystal films on *c*-plane sapphire ($0 \leq x \leq 1$). The authors utilized Tauc plots to estimate the direct and indirect bandgap, respectively. Additionally, they applied Tauc–Lorentz and O'Leary–Johnson–Lim models to derive bandgap values.[27] Uchida *et al.* analyzed a set of mist-CVD grown samples ($0 \leq x \leq 1$) using x-ray photoelectron spectroscopy. The bandgaps were determined using the energy loss spectrum of the O 1s core level, finding a bowing parameter of 1.52 eV.[28] Chen *et al.* also applied an x-ray photoelectron spectroscopy approach to determine the bandgap for a set of pulsed laser deposition films on *a*-plane sapphire ($0 \leq x \leq 1$), obtaining a bowing parameter of 1.59 eV.[21] Xia *et al.* deposited α-$(Al_xGa_{1-x})_2O_3$ using combinatorial pulsed laser deposition approach for samples with concentration from $0.26 \leq x \leq 0.74$, and x-ray photoelectron spectroscopy was used to determine bandgap values with an associated bowing parameter of 3 eV.[23] Jinno *et al.* evaluated PAMBE grown thin films on *m*-plane sapphire ($0 \leq x \leq 1$) using unpolarized transmission measurements determining a bowing parameter of 1.1 eV.[24] No polarization sensitive measurements were reported for α-$(Al_xGa_{1-x})_2O_3$ thin films suitable to differentiate the anisotropic optical properties and, thus, the direction dependent bandgap parameters.

Mueller matrix spectroscopic ellipsometry is a widely used technique for determining the dielectric function tensor and associated critical point (CP) transitions of anisotropic thin films.[16,29–34] Studies investigating the α-phase bandgap are reported for Ga_2O_3.[6,35–37] An α-$(Al_xGa_{1-x})_2O_3$ thin film investigation in the below-bandgap spectral range was performed by Hilfiker *et al.* The high-frequency dielectric constants and transparent region dielectric functions (1–4.5 eV) were determined using a Cauchy model analysis of Mueller matrix spectroscopic ellipsometry data for a set of PAMBE single-crystal thin films on *m*-plane sapphire ($0 \leq x \leq 1$).[38] Spectroscopic ellipsometry requires a model-based approach to determine the optical properties of a material, ideally in combination with DFT computations. In this Letter, we expand on our previous approach for α-Ga_2O_3[6] and determine the anisotropic dielectric function tensor, CP transitions, and excitonic contributions. From this information, we determine the bandgap order, characteristics, and bandgap composition parameters including anisotropy for single crystalline α-$(Al_xGa_{1-x})_2O_3$ thin films ($0 \leq x \leq 1$).

α-$(Al_xGa_{1-x})_2O_3$ thin films were epitaxially grown on sapphire substrates using PAMBE. The thin films maintain the same crystallographic orientation of the underlying *m*-plane sapphire substrate. The full sample set was fabricated using an oxygen flow rate of 0.50 sccm and a radio frequency plasma source ($RF_{power} = 250$ W) with substrate temperatures of 650 °C ($x < 1$) and 750 °C ($x = 1$). All thin films are mostly strain free as determined from asymmetrical reciprocal space maps. Further structural characterization and fabrication information are detailed in Ref. 24.

Mueller matrix spectroscopic ellipsometry data were acquired at various azimuthal rotations, thereby resolving both the perpendicular

($\varepsilon_\perp$) and parallel to lattice direction c polarized dielectric functions ($\varepsilon_\parallel$). Note that both polarization directions are contained in the sample surface plane. We define the corresponding dielectric function tensor such that Euler angle rotations as detailed in Ref. 39 can be applied to specify the sample orientation in accordance with the ellipsometer setup,[30]

$$\varepsilon = \begin{pmatrix} \varepsilon_\perp & 0 & 0 \\ 0 & \varepsilon_\perp & 0 \\ 0 & 0 & \varepsilon_\parallel \end{pmatrix}. \tag{2}$$

Each sample was analyzed across the spectral range of 5 to 8.75 eV extending analysis of data reported previously for the below-bandgap range. Each measurement was performed at room temperature with a rotating analyzer ellipsometer with an automated compensator function (VUV-VASE J.A. Woollam Co., Inc.), permitting the acquisition of the Mueller matrix excluding the fourth row. Measurements were performed at azimuthal rotations of 45° steps and at angles of incidence $\Phi_a = 50°$, 60°, and 70°.

We apply a substrate-thin film-ambient approach for data analysis. A surface roughness layer is also included. The latter is defined through an effective medium approximation, containing a 50/50 mixture of the optical constants of ambient (air) and an isotropic average of the underlying α-$(Al_xGa_{1-x})_2O_3$ thin film. Initially, the thin film (d_t) and roughness (d_r) thickness parameters are determined through a Cauchy dispersion analysis, where solely the sub-bandgap transparent region of each material is analyzed. This analysis is discussed in detail in Ref. 38. Subsequently, the so-called "wavelength-by-wavelength" dielectric function tensor for each α-$(Al_xGa_{1-x})_2O_3$ film is determined using a regression analysis for the best matching parameters $\varepsilon_\perp$ and $\varepsilon_\parallel$ without any line shape assumptions, also known as, a point-by-point (PBP) fit. Functions $\varepsilon_\perp$ and $\varepsilon_\parallel$ for the m-plane sapphire substrate were determined separately through measurement and analysis of an individual substrate and assumed to be the same across the full sample set. Then, functions for $\varepsilon_\perp$ and $\varepsilon_\parallel$ are analyzed further using a CP model dielectric function (MDF) approach to analyze the band-to-band transitions and excitonic features. For polarization perpendicular to the lattice c direction the first two band-to-band transitions contributing to $\varepsilon_\perp$ are described using the M_0-type CP-MDF line shape[25,39,40]

$$\varepsilon_{(M_0)} = AE^{-1.5}\chi^{-2}\left[2-(1+\chi)^{0.5}-(1-\chi)^{0.5}\right], \tag{3}$$

$$\chi = \frac{(\hbar\omega + i\Gamma)}{E}, \tag{4}$$

where the CP amplitude, broadening, and center transition energy are denoted by A, Γ, and E, respectively. Here, $\hbar\omega$ represents the photon energy. Previous DFT and spectroscopic ellipsometry analysis of α-Ga_2O_3 determined that $\varepsilon_\parallel$ required an M_1-type CP-MDF to accurately represent the contributions from the lowest band-to-band transition, reflecting a saddle point in the joint density of states[6,39,41]

$$\varepsilon_{(M_1)} = -\frac{A}{\chi^2} ln\left[1-\chi^2\right]. \tag{5}$$

Note that for $x = 0.59$ the lowest band-to-band transition in $\varepsilon_\parallel$ is an M_0-type CP. As will be explained further below, this is due to the change in valence band order and curvature. Both $\varepsilon_\perp$ and $\varepsilon_\parallel$ exhibit strong excitonic contributions at energies below the lowest band-to-band transitions. Each excitonic contribution is represented by an anharmonically broadened Lorentz oscillator

$$\varepsilon_{(ex)} = \frac{A^2 - ib\hbar\omega}{E^2 - (\hbar\omega)^2 - i\Gamma\hbar\omega}, \tag{6}$$

where b is the anharmonic broadening term which renders the asymmetric line shape of the exciton contributions to the dielectric function. This form has been widely used for ultra-wide bandgap materials. The form was introduced by Mock *et al.* for β-Ga_2O_3 in Ref. 33. A detailed discussion of the presentation of the anharmonically broadened oscillator form suggested by Gervais and Piriou in Ref. 42 and the form suggested by Mock *et al.* in Ref. 43 has yet to appear in the literature. Briefly, simple mathematical transformations prove that both forms are identical. The advantage of the latter form, Eq. (6) in this paper, is that it can be added to a sum of model contributions to the dielectric function, while the former must be brought into a product form considerably complicating the regression calculations. A recent temperature-dependent observation of the exciton dissociation demonstrated validation of this form for zinc gallate, for example.[44] In our previous combined density functional theory and ellipsometry analysis of α-Ga_2O_3, we found the M_0 CP in the perpendicular to c polarization is associated with an effective three-dimensional hydrogen atom-like exciton, containing an exciton binding energy of 7 meV. This differs from the parallel to c polarization, where the M_1 CP is described with a two-dimensional hydrogen-like exciton, leading to a higher exciton binding energy of 178 meV. Each exciton binding energy is anticipated to change with increasing aluminum concentration. Higher energy transitions occur in close spectral energy proximity to one another leading to a difficulty in differentiating individual CP contributions. Instead, these transitions are represented through a Gaussian broadened oscillator in the imaginary ($\Im$) part of the dielectric function

$$\Im\{\varepsilon_{(G)}\} = A\left(e^{-\left[\frac{\hbar\omega-E}{\sigma}\right]^2} - e^{-\left[\frac{\hbar\omega+E}{\sigma}\right]^2}\right), \tag{7}$$

$$\sigma = \Gamma/(2\sqrt{ln(2)}). \tag{8}$$

Kramers–Kronig integration is applied to the Gaussian oscillator to obtain the real part[29,39]

$$\Re\{\varepsilon_{(G)}\} = \frac{2}{\pi} P\int_0^\infty \frac{\xi\Im\{\varepsilon_{(G)}\}}{\xi^2 - (\hbar\omega)^2} d\xi. \tag{9}$$

As x increases, the higher-energy transitions shift to higher photon energies, eventually beyond the measurement range. Therefore, the center energies of the higher energy transitions cannot be determined in this Letter, and we need to make an assumption about their behaviors. We have, thus, fixed these to occur at the same spectral energy distance from the lowest band-to-band transition at which they occur in α-Ga_2O_3.

The PBP and CP-MDF for $\varepsilon_\perp$ and $\varepsilon_\parallel$ are shown in the supplementary material. Plots of PBP and MDF are virtually indistinguishable, indicating an excellent model fit. In both directions, a narrowing of the peak in the dielectric function is noted for increasing Al content. This can be attributed to a decrease in the broadening of the exciton contribution. Additionally, in the perpendicular to c polarization

direction, the amplitude of the second lowest band-to-band transition ($E_{1,\perp}$) decreases as the Al content increases until it fully disappears for 59% Al. The MDF parameters are given in Table I.

The dielectric functions determined from the spectroscopic ellipsometry PBP approach are shown in Fig. 1. The sapphire optical constants shown in black dashed lines are measured from a commercial sapphire substrate and are in excellent agreement with the dielectric function determined for the PAMBE grown α-Al_2O_3 film. A decrease in the birefringence is evident as the aluminum content increases. Furthermore, a sharper change in the dielectric function in the bandgap region occurs for higher aluminum content films.

TABLE I. $\varepsilon_\perp$ and $\varepsilon_\parallel$ best-match CP MDF parameters for α-$(Al_xGa_{1-x})_2O_3$ thin films. Values for $\varepsilon_{off,\perp}$ and $\varepsilon_{off,\parallel}$ are also given. 90% confidence interval is indicated with the final digit in parentheses.

CP	Equation No.	A	E (eV)	Γ (eV)	b (eV)
$\varepsilon_\perp$, $x = 0.18$, $\varepsilon_{off,\perp} = 1.208(9)$					
$CP^{(0x)}$	(6)	1.18(9)	5.86(0)	0.60(5)	0.14(5)
$CP^{(0)}$	(3) and (4)	61.(3)	5.86(7)	0.07(9)	⋯
$CP^{(1)}$	(3) and (4)	33.(9)	6.44(6)	0.11(1)	⋯
$CP^{(2)}$	(7)–(9)	4.70(3)	10.68(9)	2.75(9)	⋯
$\varepsilon_\parallel$, $x = 0.18$, $\varepsilon_{off,\parallel} = 0.61(8)$					
$CP^{(0x)}$	(6)	0.64(2)	5.88(1)	0.797(8)	0.66(9)
$CP^{(0)}$	(4) and (5)	0.38(6)	5.94(9)	0.52(8)	⋯
$CP^{(1)}$	(7)–(9)	2.64(4)	9.6(1)	0.78(5)	⋯
$CP^{(2)}$	(7)–(9)	3.66(0)	11.5(6)	6.4(9)	⋯
$\varepsilon_\perp$, $x = 0.37$, $\varepsilon_{off,\perp} = 1.01(2)$					
$CP^{(0x)}$	(6)	2.14(6)	6.69(2)	1.02(4)	0.96(6)
$CP^{(0)}$	(3) and (4)	71.(2)	6.69(9)	8.03(8)	⋯
$CP^{(1)}$	(3) and (4)	57.(8)	7.29(8)	0.10(4)	⋯
$CP^{(2)}$	(7)–(9)	4.92(1)	11.5(4)	3.6(3)	⋯
$\varepsilon_\parallel$, $x = 0.37$, $\varepsilon_{off,\parallel} = 0.39(9)$					
$CP^{(0x)}$	(6)	1.8(6)	6.65(9)	0.93(3)	1.0(2)
$CP^{(0)}$	(4) and (5)	0.31(4)	6.65(9)	3.54(7)	⋯
$CP^{(1)}$	(7)–(9)	2.64(4)	10.3(2)	0.78(5)	⋯
$CP^{(2)}$	(7)–(9)	4.3(9)	12.2(7)	6.1(2)	⋯
$\varepsilon_\perp$, $x = 0.59$, $\varepsilon_{off,\perp} = 0.63(9)$					
$CP^{(0x)}$	(6)	1.2(5)	7.31(8)	0.35(8)	0.33(6)
$CP^{(0)}$	(3) and (4)	141.(9)	7.31(8)	0.78(9)	⋯
$CP^{(2)}$	(7)–(9)	4.3(1)	12.1(4)	2.7(2)	⋯
$\varepsilon_\parallel$, $x = 0.59$, $\varepsilon_{off,\parallel} = 0.19(6)$					
$CP^{(0x)}$	(6)	1.0(2)	7.32(3)	0.34(2)	0.29(3)
$CP^{(0)}$	(3) and (4)	0.14(8)	7.32(3)	0.72(8)	⋯
$CP^{(2)}$	(7)–(9)	5.1(2)	12.9(3)	6.4(0)	⋯

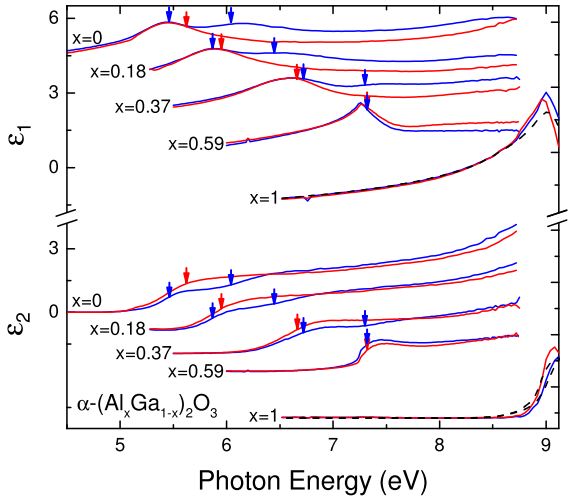

FIG. 1. Point-by-point data inversion determined real (ε_1) and imaginary (ε_2) parts of the dielectric functions for $\varepsilon_\perp$ (blue solid lines) and $\varepsilon_\parallel$ (red solid lines) for α-$(Al_xGa_{1-x})_2O_3$ thin films grown using PAMBE. Black dashed lines indicate sapphire substrate for reference. Energies for the band-to-band CP transitions are indicated with blue and red arrows, accordingly. Spectra for different Al concentration are shifted subsequently by (−1) for clarity. For $x = 1$, an offset of (−5) from $x = 0$ is applied.

Figure 2 compares the valence band structure calculated using hybrid-level DFT for α-Ga_2O_3 and α-Al_2O_3. Details for α-Ga_2O_3 were discussed in Ref. 6. For α-Al_2O_3, the calculation procedure was the same. We used the plane wave code Quantum ESPRESSO[45,57] and a combination of generalized-gradient-approximation (GGA) density functional of Perdew, Burke, and Ernzerhof[46] (PBE) and norm-conserving Fritz-Haber Institute Troullier-Martins pseudopotentials[47,48] from the Quantum ESPRESSO pseudopotentials library. The pseudopotential for gallium did not include the semicore 3*d* states in the valence configuration. All calculations were performed with a high electronic wavefunction cutoff of 400 Ry. The structures were first relaxed to force levels less than 10^{-6} Ry $Bohr^{-1}$. A dense shifted 8 × 8 × 8 Monkhorst–Pack[49] grid was used for sampling of the Brillouin zone, and a convergence threshold of 1×10^{-12} Ry was used to reach self-consistency. The hybrid-DFT calculations were performed at the PBE equilibrium geometries using the hybrid Gau-PBE[50,51] density functional and a regular non-shifted 8 × 8 × 8 Monkhorst–Pack grid for the Brillouin zone sampling and 4 × 4 × 4 grid for sampling of the Fock operator. Finally, the high-resolution interpolated band structures, for the purpose of the current study limited to 18 upper valence bands, were obtained by utilizing the band interpolation method based on the maximally localized Wannier functions[52,53] as implemented in the software package WANNIER90.[54] As the initial projections for the Wannier functions, we used *p*-type states on O atoms. As a result, we obtained 18 localized Wannier functions for each material with the spreads < 1.0 Å^2. In α-Ga_2O_3, the valence band maximum occurs on the Γ–*X* line in the Brillouin zone. However, α-Al_2O_3 is a direct bandgap material with the valence band maximum occurring at the Γ-point. Hence, the transition from indirect to direct characteristic must occur at some *x*. Furthermore, as can be seen in Fig. 2, the order of the valence bands at the top of the Γ point changes. Note that one band is

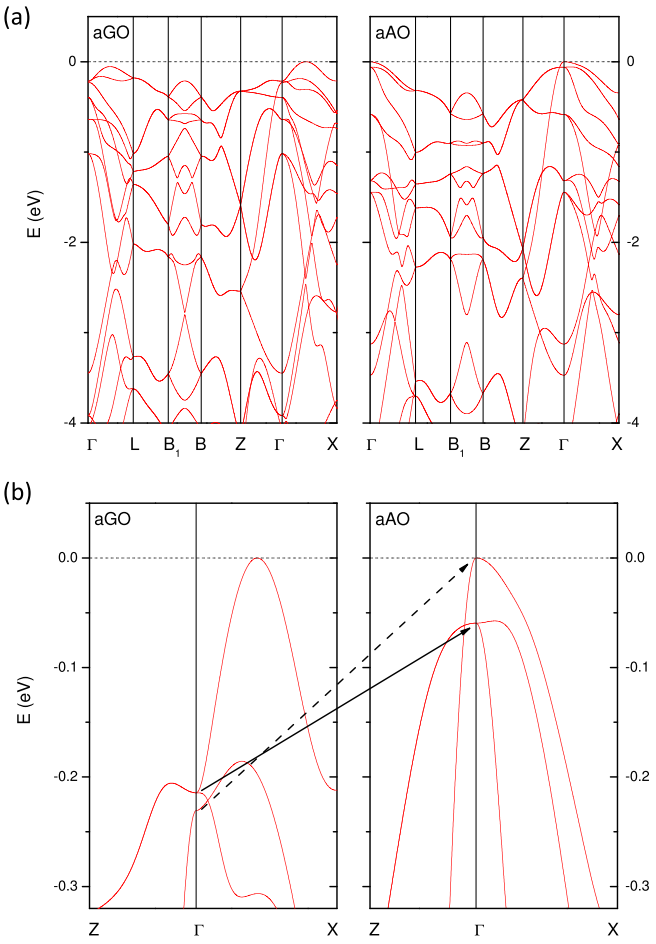

FIG. 2. (a) Hybrid-level-DFT structure of the valence bands for α-Ga_2O_3 and α-Al_2O_3 and (b) an enlarged portion of the top of the valence band around the Γ point. Each plot is shifted so the valence band maximum occurs at $E = 0$. Note that the valence band maximum occurs for α-Ga_2O_3 on the Γ–X line whereas for α-Al_2O_3 at the Γ point. Arrows in (b) indicate the evolution of the valence bands of the same symmetry, i.e., the same bands in both compounds. Bands indicated by the dashed arrow belong to the transition polarized parallel to lattice direction *c*, bands indicated by the solid arrows belong to polarization perpendicular to *c*. The bottom of the conduction band at the Γ-point is isotropic and parabolic. It was discussed in detail previously in Ref. 6 and is not shown here. Labeling of high symmetry points as in Ref. 55.

doubly degenerate at the Γ point, and the associated transition to the conduction band belongs to "⊥", while the other valence band level is formed by a single band and belongs to "‖". Furthermore, for $x = 0$, the double degenerate band is hyperbolic (the curvature from Γ toward X is negative, while the curvature toward Z is positive) and for $x = 1$, both curvatures are positive. Accordingly, for $x = 0$, the associated band-to-band transition CP-MDF is of M_1-type while for $x = 1$, it is of M_0-type. Hence, direct–indirect characteristics, band order, and band curvatures must change at some aluminum content between α-Ga_2O_3 and α-Al_2O_3. These compositions are unknown.

In Fig. 3, we show the lowest band-to-band transition CP energy parameter for parallel and perpendicular to *c* polarization from our

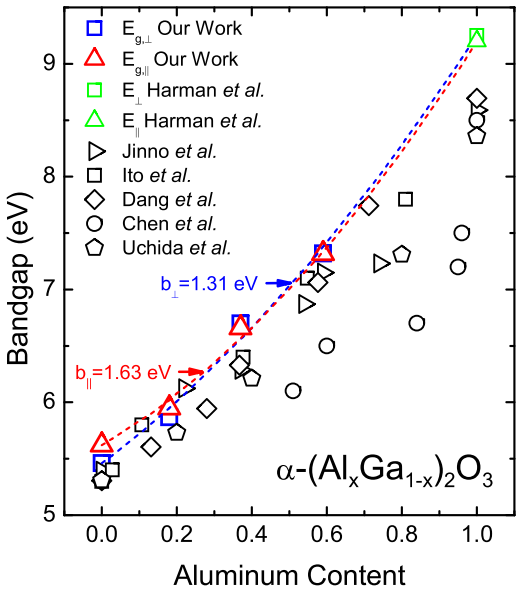

FIG. 3. Lowest band-to-band transition energies for perpendicular to *c* polarization direction (blue squares) and parallel to *c* (red triangles) direction determined in this Letter. Dashed lines represent the best-fit quadratic fit with associated bowing parameters. Previously obtained bandgap energies are indicated by black open symbols. Note that Harman *et al.*,[8] Jinno *et al.*,[20] Ito *et al.*,[19] Dang *et al.*,[27] Harman *et al.*,[21] and Uchida *et al.*[28] ignored band order and anisotropy.

modeling approach. We note that our spectroscopic ellipsometry analysis is unable to determine the CP transitions in α-Al_2O_3, as their contributions occur at the boundary of the measurement range. Therefore, we augment the bandgap values determined by Harman *et al.*[8] Note that the data from Harman *et al.* were not obtained from a MDF approach and may be rather seen as best estimates at this point. Accurate analysis of the sapphire bandgap, its anisotropy, and excitonic contributions have not been reported yet. Then, we use the lowest CP transition energy parameters in Table I and Eq. (1) and fit bowing parameters ($b_{Eg,\perp} = 1.31$ eV and $b_{Eg,\|} = 1.61$ eV). Table II summarizes bowing parameters determined from previous investigations where anisotropy was ignored throughout. Using our bowing parameters, we observe a crossover in the valence band order at approximately 40% Al concentration. This is indicative of a degeneracy point in the band structure, where there exists a change in valence band order with respect to their optical polarization direction. Furthermore, a shift must occur between the indirect nature of α-Ga_2O_3 and the direct α-Al_2O_3. This shift is likely to occur at the same 40% Al concentration. The argument in support of this expectation is the following: The band structure must transform conformal between the two compounds because it is the same crystal structure. Only elemental changes occur. The bands that are degenerate at Γ, i.e., the ones associated with "⊥" transitions, form a side maximum away from Γ toward X in the Brillouin zone. See Fig. 2. But these bands do not cross along the direction from Γ to X with the band associated with the "‖" transition. Hence, by simple topological argument, when the nondegenerate band shifts over the degenerate band (from $x = 0$ toward $x = 1$ at about 40%) at the Γ point, the side maximum within the degenerate band must be at least slightly below the Γ point

TABLE II. Comparison of bowing parameters obtained through theoretical and experimental investigations for α-$(Al_xGa_{1-x})_2O_3$. Note, this work obtained the bowing parameters separately for $\varepsilon_\perp$ and $\varepsilon_{||}$.

Author	Reference	Growth method	Measurement technique	b_{Eg} (eV)
This work	···	PAMBE	Ellipsometry	(⊥) 1.31
This work	···	PAMBE	Ellipsometry	(‖) 1.61
Wang *et al.*	26	···	DFT	1.6
Peelaers *et al.*	17	···	DFT	1.87
Jinno *et al.*	24	PAMBE	Transmittance	1.1
Uchida *et al.*	28	Mist-CVD	XPS	1.52
Chen *et al.*	21	Pulsed Laser Deposition (PLD)	XPS	1.59
Xia *et al.*	23	PLD	XPS	3
Dang *et al.*	27	Mist-CVD	Transmittance[a,b,c,d]	0.84–2.10

[a]0.84 eV—determined from direct bandgap Tauc plots.
[b]1.30 eV—obtained through O'Leary–Johnson–Lim model.
[c]1.62 eV—determined from indirect bandgap Tauc plots.
[d]2.10 eV—obtained through Tauc–Lorentz model.

maximum of the nondegenerate band; otherwise, it would cross the nondegenerate band somewhere along the line from Γ to X. As stated above, DFT calculations indicate all here considered CP transitions in α-Al_2O_3 are M_0-type due to their parabolic bands. Therefore, in $\varepsilon_{||}$, a composition must exist where the nature of the lowest CP shifts from M_1-type to M_0-type. This is probable to also occur at the 40% Al concentration, where the order change in the valence bands also switch between indirect to direct nature. Accordingly, we model the lowest CP in $\varepsilon_{||}$ for the 59% Al thin film using an M_0-type MDF.

In summary, a Mueller matrix spectroscopic ellipsometry approach was applied to determine a CP-MDF for the anisotropic PAMBE grown α-$(Al_xGa_{1-x})_2O_3$ thin films on *m*-plane sapphire. We determine the anisotropic band-to-band transitions and bandgap bowing parameters. Our DFT calculations indicate transformations occurring between α-Ga_2O_3 and α-Al_2O_3. A crossover in the valence band order results in a change in lowest band-to-band transition direction, a switch from indirect-gap α-Ga_2O_3 to direct-gap α-Al_2O_3 will happen, and α-Ga_2O_3 is described with an M_1-type CP in the parallel to *c* direction while the parabolic bands of α-Al_2O_3 indicate a transformation will occur to an M_0-type transition. Using the bandgap bowing parameters, we estimate that all transformations will occur at approximately 40% Al concentration.

See the supplementary material for experimental and best-match model Mueller matrix data along with all the numerical values of model-based parameters determined from this work.

This work was supported, in part, by the National Science Foundation (NSF) under Award Nos. NSF DMR 1808715 and NSF/EPSCoR, by RII Track-1: Emergent Quantum Materials and Technologies (EQUATE) under Award No. OIA-2044049, by Air Force Office of Scientific Research under Award Nos. FA9550-18-1-0360, FA9550-19-S-0003, and FA9550-21-1-0259, by ACCESS, an AFOSR Center of Excellence, under Award No. FA9550-18-1-0529, and by the Knut and Alice Wallenbergs Foundation award "Wide-bandgap semiconductors for next generation quantum components." M. Schubert acknowledges the University of Nebraska Foundation and the J. A. Woollam Foundation for financial support. R.J. acknowledges the support by the Japan Society for the Promotion of Science Overseas Challenge Program for Young Researchers 1080033. DFT calculations were, in part, performed at the Holland Computing Center of the University of Nebraska, which receives support from the Nebraska Research Initiative.

AUTHOR DECLARATIONS

Conflict of Interest

The authors have no conflicts to disclose.

DATA AVAILABILITY

The data that support the findings of this study are available from the corresponding author upon reasonable request.

REFERENCES

[1]For a definition of the hexagonal and rhombohedral crystallographic unit cells for α-Ga_2O_3, see Stokey *et al.* (Ref. 56), for monoclinic β-Ga_2O_3 see, e.g., Mock *et al.* (Ref. 33).
[2]M. Higashiwaki and G. H. Jessen, Appl. Phys. Lett. **112**, 060401 (2018).
[3]H. Zhou, J. Zhang, C. Zhang, Q. Feng, S. Zhao, P. Ma, and Y. Hao, J. Semicond. **40**, 011803 (2019).
[4]D. Shinohara and S. Fujita, Jpn. J. Appl. Phys., Part 1 **47**, 7311 (2008).
[5]J. A. Spencer, A. L. Mock, A. G. Jacobs, M. Schubert, Y. Zhang, and M. J. Tadjer, Appl. Phys. Rev. **9**, 011315 (2022).
[6]M. Hilfiker, R. Korlacki, R. Jinno, Y. Cho, H. G. Xing, D. Jena, U. Kilic, M. Stokey, and M. Schubert, Appl. Phys. Lett. **118**, 062103 (2021).
[7]O. Slobodyan, J. Flicker, J. Dickerson, J. Shoemaker, A. Binder, T. Smith, S. Goodnick, R. Kaplar, and M. Hollis, J. Mater. Res. **37**, 849 (2022).
[8]A. K. Harman, S. Ninomiya, and S. Adachi, J. Appl. Phys. **76**, 8032 (1994).
[9]S. Mu, H. Peelaers, and C. G. Van de Walle, Appl. Phys. Lett. **115**, 242103 (2019).
[10]U. Mishra, P. Parikh, and Y.-F. Wu, Proc. IEEE **90**, 1022 (2002).
[11]J. M. Redwing, D. A. S. Loeber, N. G. Anderson, M. A. Tischler, and J. S. Flynn, Appl. Phys. Lett. **69**, 1 (1996).
[12]Z. Alaie, S. M. Nejad, and M. Yousefi, Mater. Sci. Semicond. Process. **29**, 16 (2015).
[13]C. G. Moe, Y. Wu, J. Piprek, S. Keller, J. S. Speck, S. P. DenBaars, and D. Emerson, Phys. Status Solidi A **203**, 1915 (2006).

[14]G. Brummer, D. Nothern, A. Y. Nikiforov, and T. D. Moustakas, Appl. Phys. Lett. **106**, 221107 (2015).
[15]A. Mauze and J. Speck, "Plasma-assisted molecular beam epitaxy 1," in *Gallium Oxide: Materials Properties, Crystal Growth, and Devices*, edited by M. Higashiwaki and S. Fujita (Springer International Publishing, Cham, 2020), pp. 79–93.
[16]M. Hilfiker, U. Kilic, A. Mock, V. Darakchieva, S. Knight, R. Korlacki, A. Mauze, Y. Zhang, J. Speck, and M. Schubert, Appl. Phys. Lett. **114**, 231901 (2019).
[17]H. Peelaers, J. B. Varley, J. S. Speck, and C. G. Van de Walle, Appl. Phys. Lett. **112**, 242101 (2018).
[18]D. S. Cook, J. E. Hooper, D. M. Dawson, J. M. Fisher, D. Thompsett, S. E. Ashbrook, and R. I. Walton, Inorg. Chem. **59**, 3805 (2020).
[19]H. Ito, K. Kaneko, and S. Fujita, Jpn. J. Appl. Phys., Part 1 **51**, 100207 (2012).
[20]R. Jinno, K. Kaneko, and S. Fujita, Jpn. J. Appl. Phys., Part 1 **60**, SBBD13 (2021).
[21]Z. Chen, M. Arita, K. Saito, T. Tanaka, and Q. Guo, AIP Adv. **11**, 035319 (2021).
[22]R. Kumaran, T. Tiedje, S. E. Webster, S. Penson, and W. Li, Opt. Lett. **35**, 3793 (2010).
[23]X. Xia, C. Fares, F. Ren, A. Hassa, H. von Wenckstern, M. Grundmann, and S. J. Pearton, ECS J. Solid State Sci. Technol. **10**, 113007 (2021).
[24]R. Jinno, C. S. Chang, T. Onuma, Y. Cho, S.-T. Ho, D. Rowe, M. C. Cao, K. Lee, V. Protasenko, D. G. Schlom, D. A. Muller, H. G. Xing, and D. Jena, Sci. Adv. **7**, eabd5891 (2021).
[25]M. Schubert, T. Hofmann, B. Rheinländer, I. Pietzonka, T. Sass, V. Gottschalch, and J. A. Woollam, Phys. Rev. B **60**, 16618 (1999).
[26]T. Wang, W. Li, C. Ni, and A. Janotti, Phys. Rev. Appl. **10**, 011003 (2018).
[27]G. T. Dang, T. Yasuoka, Y. Tagashira, T. Tadokoro, W. Theiss, and T. Kawaharamura, Appl. Phys. Lett. **113**, 062102 (2018).
[28]T. Uchida, R. Jinno, S. Takemoto, K. Kaneko, and S. Fujita, Jpn. J. Appl. Phys., Part 1 **57**, 040314 (2018).
[29]H. Fujiwara, *Spectroscopic Ellipsometry* (John Wiley & Sons, New York, 2007).
[30]M. Schubert, *Handbook of Ellipsometry*, edited by E. Irene and H. Tompkins (William Andrew Publishing, 2004).
[31]M. Hilfiker, M. Stokey, R. Korlacki, U. Kilic, Z. Galazka, K. Irmscher, S. Zollner, and M. Schubert, Appl. Phys. Lett. **118**, 132102 (2021).
[32]C. Sturm, J. Furthmüller, F. Bechstedt, R. Schmidt-Grund, and M. Grundmann, APL Mater. **3**, 106106 (2015).
[33]A. Mock, R. Korlacki, C. Briley, V. Darakchieva, B. Monemar, Y. Kumagai, K. Goto, M. Higashiwaki, and M. Schubert, Phys. Rev. B **96**, 245205 (2017).
[34]C. Sturm, R. Schmidt-Grund, C. Kranert, J. Furthmüller, F. Bechstedt, and M. Grundmann, Phys. Rev. B **94**, 035148 (2016).
[35]M. Kracht, A. Karg, M. Feneberg, J. Bläsing, J. Schörmann, R. Goldhahn, and M. Eickhoff, Phys. Rev. Appl. **10**, 024047 (2018).
[36]A. Segura, L. Artús, R. Cuscó, R. Goldhahn, and M. Feneberg, Phys. Rev. Mater. **1**, 024604 (2017).
[37]M. Feneberg, J. Nixdorf, M. D. Neumann, N. Esser, L. Artús, R. Cuscó, T. Yamaguchi, and R. Goldhahn, Phys. Rev. Mater. **2**, 044601 (2018).
[38]M. Hilfiker, U. Kilic, M. Stokey, R. Jinno, Y. Cho, H. G. Xing, D. Jena, R. Korlacki, and M. Schubert, Appl. Phys. Lett. **119**, 092103 (2021).
[39]J. A. Woollam Co., Inc., *Guide to Using WVASE® Spectroscopic Ellipsometry Data Acquisition and Analysis Software* (J. A. Woollam Co., Inc., Lincoln, NE, 2012).
[40]P. Yu and M. Cardona, *Fundamentals of Semiconductors* (Springer, Berlin, 1999).
[41]K. Strössner, S. Ves, and M. Cardona, Phys. Rev. B **32**, 6614 (1985).
[42]F. Gervais and B. Piriou, J. Phys. C **7**, 2374 (1974).
[43]A. Mock, R. Korlacki, S. Knight, M. Stokey, A. Fritz, V. Darakchieva, and M. Schubert, Phys. Rev. B **99**, 184302 (2019).
[44]M. Hilfiker, E. Williams, U. Kilic, Y. Traouli, N. Koeppe, J. Rivera, A. Abakar, M. Stokey, R. Korlacki, Z. Galazka, K. Irmscher, and M. Schubert, Appl. Phys. Lett. **120**, 132105 (2022).
[45]P. Giannozzi, S. Baroni, N. Bonini, M. Calandra, R. Car, C. Cavazzoni, D. Ceresoli, G. L. Chiarotti, M. Cococcioni, I. Dabo, A. D. Corso, S. de Gironcoli, S. Fabris, G. Fratesi, R. Gebauer, U. Gerstmann, C. Gougoussis, A. Kokalj, M. Lazzeri, L. Martin-Samos, N. Marzari, F. Mauri, R. Mazzarello, S. Paolini, A. Pasquarello, L. Paulatto, C. Sbraccia, S. Scandolo, G. Sclauzero, A. P. Seitsonen, A. Smogunov, P. Umari, and R. M. Wentzcovitch, J. Phys.: Condens. Mater. **21**, 395502 (2009).
[46]J. P. Perdew, K. Burke, and M. Ernzerhof, Phys. Rev. Lett. **77**, 3865 (1996).
[47]M. Fuchs and M. Scheffler, Comput. Phys. Commun. **119**, 67 (1999).
[48]N. Troullier and J. L. Martins, Phys. Rev. B **43**, 1993 (1991).
[49]H. J. Monkhorst and J. D. Pack, Phys. Rev. B **13**, 5188 (1976).
[50]J.-W. Song, K. Yamashita, and K. Hirao, J. Chem. Phys. **135**, 071103 (2011).
[51]J.-W. Song, G. Giorgi, K. Yamashita, and K. Hirao, J. Chem. Phys. **138**, 241101 (2013).
[52]N. Marzari and D. Vanderbilt, Phys. Rev. B **56**, 12847 (1997).
[53]I. Souza, N. Marzari, and D. Vanderbilt, Phys. Rev. B **65**, 035109 (2001).
[54]A. A. Mostofi, J. R. Yates, Y.-S. Lee, I. Souza, D. Vanderbilt, and N. Marzari, Comput. Phys. Commun. **178**, 685 (2008).
[55]W. Setyawan and S. Curtarolo, Comput. Mater. Sci. **49**, 299 (2010).
[56]M. Stokey, R. Korlacki, M. Hilfiker, S. Knight, S. Richter, V. Darakchieva, R. Jinno, Y. Cho, H. G. Xing, D. Jena, Y. Oshima, K. Khan, E. Ahmadi, and M. Schubert, Phys. Rev. Mater. **6**, 014601 (2022).
[57]See http://quantum-espresso.org for Quantum ESPRESSO wave code.